Journal of Materials Chemistry A

Accepted Manuscript

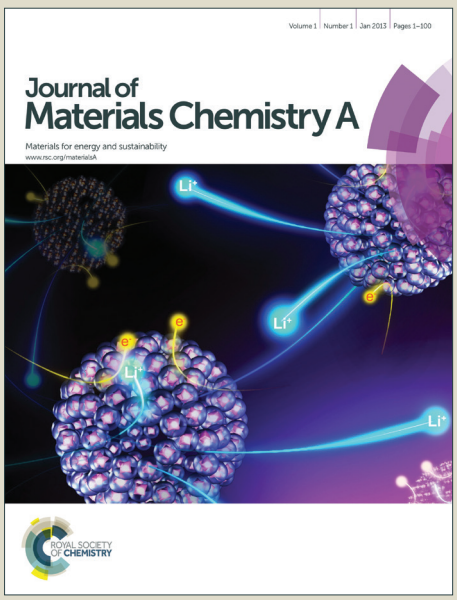

ROYAL SOCIETY OF CHEMISTRY

www.rsc.org/materialsA

Optical, Electronic, and Photoelectrochemical Properties of the *p*-type $Cu_{3-x}VO_4$ Semiconductor

Prangya P. Sahoo, Brandon Zoellner and Paul A. Maggard*

Department of Chemistry, North Carolina State University, Raleigh, NC 27695-8204

*Corresponding Author:
Paul A. Maggard, Department of Chemistry
North Carolina State University
Raleigh, NC 27695-8204
Phone: (+1) 919-515-3616

I. ABSTRACT

Investigations into new *p*-type metal oxides with small bandgap sizes, i.e., E_g ~0.9 eV to ~1.5 eV, are currently needed to enable the preparation of tandem cells with high solar-to-hydrogen conversion efficiencies. The *p*-type Cu(I)-vanadate, Cu_3VO_4 (space group *I*-42*m* (No. 121), $Z = 2$, $a = 4.581(4)$ Å, $c = 8.998(2)$ Å), was synthesized in high purity using solid-state methods and investigated for its small optical bandgap size (E_g ~ 1.2 eV) and photoelectrochemical properties in the form of polycrystalline films. Powder X-ray diffraction and electron microscopy data show that, beginning at 300 ^oC in air, a Cu-deficient composition is formed according to: $Cu_3VO_4(s) + (x/2)\ O_2(g) \rightarrow Cu_{3-x}VO_4(s) + x\ CuO(s)$. At 350 ^oC the compound decomposes at the surfaces into the Cu(II)-containing oxides CuO and $Cu_3V_2O_8$ (3:1 molar ratio), the latter protruding as rods (i.e., ~15-25 nm in width by ~1-5μm in length) from the particles' surfaces. Polycrystalline films of *p*-type Cu_3VO_4 were prepared under these conditions (i.e., heated in air at 300 ^oC or 350 ^oC) and found to yield significant cathodic photocurrents under solar-simulated, visible-light irradiation ($\lambda > 420$ nm; AM 1.5 G filter, irradiant power density of ~100mW/cm^2). Their photocurrents increased with the heating

temperature of the film and with the applied bias, e.g., ~0.1 mA/cm^2 at zero applied bias to ~0.25 mA/cm^2 at -0.2 applied bias (pH = 5.8). The photocurrent of a non-heated film was negligible compared to the films heated in air and exhibited a larger dark current. Further, when CuO nanoparticles were formed directly onto the Cu_3VO_4 films from aqueous $Cu(NO_3)_2$ solutions (i.e., 0.1 M and 0.25 M), cathodic photocurrents of ~0.2 mA/cm^2 are similarly found. Mott-Schottky measurements determined the energetic potential of the Cu_3VO_4 conduction band to be at ~ –0.63V versus RHE at pH = 5.8, with an acceptor concentration of ~1.29×10^{17} cm^{-3}. Thus, a type-II band offset is predicted to occur between the *p*-type Cu_3VO_4 film and the *p*-type CuO surface nanoparticles, and elucidating the critical role of the CuO surface nanoparticles in forming a charge rectification barrier and enhancing the charge separation at the surfaces. Electronic structure calculations show that the conduction band states of Cu_3VO_4 are delocalized within the *ab*-plane of the structure and exhibit an ~2 eV band dispersion centered around the gamma *k*-point. The bandgap size, conduction band dispersion, and band energies of Cu_3VO_4 are thus found to be promising for further investigations into tandem *n*-/*p*-type photoelectrochemical cells for solar energy conversion applications.

II. INTRODUCTION

The efficient conversion of solar energy into chemical fuels using stable semiconductor photoelectrodes has been a subject of intense investigation over the past few decades in the field of photoelectrochemistry. [1-5] As nearly 50% of the incident solar energy on the Earth's surface falls within the visible-light energy range, recent research has focused on the synthesis and

development of *n*-type and *p*-type metal-oxide photoelectrodes capable of absorbing visible light. Large bandgap metal oxides, such as widely used *n*-type TiO_2, are promising in terms of their robustness against photocorrosion in aqueous solutions under irradiation. Relatively fewer *n*-type metal oxides with small visible-light bandgap sizes have been investigated for water oxidation, such as α-Fe_2O_3 or WO_3.[6-7] The decrease in bandgap size in these cases arises from lowered conduction band energies (i.e., to less negative potentials), and typically making these types of metal-oxides unsuitable for use as *p*-type photoelectrodes in the reduction of water or carbon dioxide. Thus, there are significantly fewer examples of *p*-type metal-oxide photoelectrodes with small visible-light bandgap sizes, such as *p*-type Cu_2O, $CaFe_2O_4$ and metal-doped Fe_2O_3, that are capable of driving fuel-producing reduction reactions from water or carbon dioxide.[8-11]

Recently, our research efforts have been directed towards the synthesis and discovery of new *p*-type Cu(I)-containing mixed-metal oxides hitherto unexplored for their solar-driven photocatalytic or photoelectrochemical properties.[4,12-17] These metal-oxide compounds have consisted of a range of structures that combine Nb(V) or Ta(V) cations with the Cu(I) cation. This combination of transition-metal cations typically yields small visible-light bandgap sizes, depending upon the specific composition and structure. Their bandgap sizes are determined by the energetic separation of the empty higher-energy d^0 orbitals and the filled lower-energy d^{10} orbitals that form the conduction and valence band, respectively. Owing to the relatively higher-energy Ta $5d^0$ orbitals, Cu(I)-tantalates have been found to exhibit larger bandgap sizes, such as found for $Cu_5Ta_{11}O_{30}$ of ~2.6 eV.[15,17] By comparison, the relatively lower-energy Nb $4d^0$ orbitals lead to smaller bandgap sizes of ~1.4 eV to ~2.0 eV, such as known for $CuNb_3O_8$ and $CuNbO_3$,[12,13] respectively. In the form of *p*-type polycrystalline photoelectrodes these metal

oxides exhibit significant cathodic photocurrents under visible-light irradiation, and which have been found to be significantly enhanced after heating in air to yield Cu-deficient compositions (i.e., $Cu_{1-x}Nb_3O_8$ and $Cu_{5-x}Ta_{11}O_{30}$) and nano-sized CuO surface islands. Recent research has shown that a thin coating (or islands) of CuO can yield increased surface protection against photocorrosion as well as higher photocurrents, such as reported for films of Cu_2O,[18,19] $CuWO_4$,[20] and $CuBi_2O_4$.[21] While the surface CuO nanoparticles are formed under specific preparation conditions in each of these cases, by contrast, it has been found for the Cu(I)-tantalates and Cu(I)-niobates that the CuO surface islands form as a result of heating in air, such as for $Cu_5Ta_{11}O_{30}$ and $CuNb_3O_8$.[22,23]

Tandem photoelectrode systems, i.e., configurations that combine *n*-type with *p*-type semiconductors, offer significant advantages in reaching higher solar-to-hydrogen efficiencies. Under realistic water-splitting conditions, the optimum pairing of semiconductors has been calculated to be a combination of bandgap sizes of ~1.5-2.0 eV with ~0.7-1.2 eV, depending upon the full set of external conditions.[24] While several *n*-type photoelectrodes are currently known that fall in the upper-energy range of these bandgap sizes, there are few to no complementary *p*-type metal-oxides at the lower-energy range of these bandgap sizes. In addition, the conduction-band energy of the *p*-type photoelectrode must be sufficiently negative to drive hydrogen production under the operating conditions. Very few materials have been found which satisfy both of these criteria. However, compounds within the Cu(I)-vanadate system have shown promise for their *p*-type conductivity as well as potentially much smaller bandgap sizes.[25,26] Herein, the optical bandgap size, band energies, and particle sizes and surfaces of Cu_3VO_4 have been characterized, with a focus on the heating conditions that can be used to prepare it in the form of *p*-type films exhibiting the largest cathodic photocurrents.

III. EXPERIMENTAL

A. Materials and Synthesis. The solid-state reactants Cu_2O and V_2O_5 (Alfa Aesar, 99.99%) were used as received. The synthesis of Cu_3VO_4 began by grinding together stoichiometric amounts of Cu_2O and V_2O_5 using an agate mortar and pestle within a glovebox. Next, these mixed reactants were added to fused-silica reaction tubes, removed from the glovebox, and then flame-sealed under dynamic vacuum on a vacuum line (pressure $\leq$ 25 mTorr). The reaction vessels were heated to 550 ºC and soaked at that temperature for 24 h. A black-colored powder of crystalline Cu_3VO_4 was obtained in high purity according to powder X-ray diffraction data (described below). In order to investigate the effects of the film preparation conditions, the Cu_3VO_4 products were also heated in alumina crucibles under a dynamic vacuum at 400 ^{o}C for 3 h, followed by heating in air at either 300 ^{o}C or 350 ^{o}C for 15 min, or at 350 ^{o}C for 120 min.

B. Characterization. Powder X-ray diffraction (XRD) data were collected for each of the Cu_3VO_4 samples at room temperature on a Rigaku R-Axis Spider diffractometer with a curved image plate detector and Cu Kα radiation from a sealed-tube X-ray source over the angular range of $10° \leq 2\theta \leq 100°$, with a step width of 0.01° at room temperature. The data were calibrated against a silicon powder (NIST-SRM 640c) standard. A *Le Bail* profile analysis in the *JANA2000* suite was used for the lattice constant refinements of the powder XRD data.[27] The background was estimated by a Legendre polynomial function consisting of 15 coefficients, and the peak shapes were described by a pseudo-Voigt function varying five profile coefficients. A scale factor, a zero error factor and shape were refined. The 2θ range of 14.5^{o} to 15.6^{o} was masked during the refinement, as the reflection at this range corresponded to the quartz capillary

used for mounting the sample. Refined lattice constants are listed in Table 1, and an example of the whole pattern fitting is given in the Supporting Information (Figures S1)

A UV-Vis diffuse reflectance spectrum was collected for each powdered sample on a Shimadzu Spectrometer UV-3600 using an integrating sphere in the wavelength range of 200 nm to 1300 nm. Approximately 20 mg of each sample was mounted onto a sample holder by pressing the powder into a $BaSO_4$ matrix and placing it along the external window of the integrating sphere. Pressed barium sulfate powder was prepared as a reference, and the data were plotted as the function $F(R) = (1-R_\infty)^2/(2R_\infty)$, where R is the diffuse reflectance based on the Kubelka-Munk theory of diffuse reflectance.[28] The absorption edge and the photon energy are related by the equation $(h\nu\alpha)^n = A(h\nu-E_g)$; where h = Planck's constant, ν = frequency of light, α = absorption coefficient, E_g = band gap, and A = proportionality constant. The value of the exponent n denotes the nature of transition, which can be $n = 2$ for a direct allowed transition, and $n = 1/2$ for an indirect allowed transition. Thus, plots of $[h\nu\alpha]^n$ against $h\nu$, i.e., Tauc plots,[29] can be used to extract the direct and indirect bandgap sizes. Tauc plots for the direct and indirect bandgap transitions of Cu_3VO_4 are provided in Figure S4 in the Supporting Information.

The Cu_3VO_4 particle morphologies, surfaces features, and chemical compositions were characterized using a JEOL JSM-6400F field-emission scanning electron microscope (SEM) and an FEI Quanta 3D FEG focused ion beam SEM. Thermogravimetric data on the Cu_3VO_4 powder were taken on a TA Instruments TGAQ50, and the data were plotted as percent weight change versus time at the temperatures of 300 ^oC or 350 ^oC.

C. Photoelectrochemical Measurements. Polycrystalline films were prepared on fluorine-doped tin oxide (FTO) glass slides (TEC-7 from Pilkington Glass Inc.). The FTO glass slides were cleaned three times by sonication in deionized water, followed by ethanol and

acetone for thirty minutes each. An area of ~1 × 1 cm^2 was masked off on the FTO slides using two layers of Scotch 3M tape. The Cu_3VO_4 powder was ground in a mortar and pestle in ethanol until the powder was dry. Next, ~15mg of the powder was sonicated in a mixture of tert-butanol:water (30:5 mL) for one minute before being drop-casted onto the exposed FTO, followed by the doctor blade method. Once the film was dry, the tape was removed and the films were annealed under vacuum at 400 ºC for 3 h. Film samples were subsequently heated in air at 300 ^oC for 15 min, or at 350 ºC for 15 min or 120 min. All electrochemical measurements were carried out in a custom-made Teflon cell with the Cu_3VO_4 polycrystalline film as the working electrode, Pt as the counter electrode, and a standard calomel reference electrode (sat. KCl). Argon gas was bubbled through the electrolyte solution (0.5 M Na_2SO_4) for 30 min before each of the measurements. The pH of the solution was adjusted using a dilute sulfuric acid solution until the pH = 5.8. All polycrystalline films were irradiated from the backside using a 250 Watt Xe arc lamp equipped with IR and AM 1.5 G filters to produce an irradiant power density of ~100 mW/cm^2 at the film surface. An electrochemical analyzer (Princeton Applied Research, PARSTAT 2263) controlled with PowerSuite software was employed to perform the photoelectrochemical measurements.

D. Electronic Structure Calculations. Electronic band-structure calculations were performed on the geometry-optimized Cu_3VO_4 crystal structure using plane-wave density functional theory within the Vienna Ab-Initio Simulation Package (VASP; ver. 4.6).[30] All calculations used the Perdew-Burke-Ernzerhof functional in the generalized gradient approximation,[31] employing the projector augmented wave method.[32] The Monkhorst-Pack scheme was used for automatic selection of *k*-points within the Brillouin zone.[33] A selection of 45 *k*-points was used for the initial energy-minimization step, followed by the automatic

selection of 225 *k*-points for a finer densities-of-states calculation. The band structure calculation followed the standard *k*-path (Γ – X – Y – Σ – Γ – Z – Σ_1 – N – P – Y_1 – Z), as previously outlined for the body-centered tetragonal crystal system for the condition of *c*-axis length > *a*-axis length.[34]

IV. RESULTS AND DISCUSSION

A. Structural Characterization and Surface Oxidation. The Cu_3VO_4 phase has been previously found to crystallize in the body-centered tetragonal crystal system (space group *I*-42*m*) with the cell parameters *a* = 4.57531(9) Å and c = 8.9918(3) Å.[25] Briefly, the structure consists of a three dimensional network of vertex-shared CuO_4 and VO_4 tetrahedra (in a 3:1 ratio) that form two types of layers, $[Cu_2O_4]_\infty$ layers and mixed-cation $[CuVO_4]_\infty$ layers that alternate down the *c*-axis, as shown in Figure 1. The latter $[CuVO_4]_\infty$ layer is illustrated in Figure 1 (left). Listed in Table 1, the refined lattice constants are consistent with the previous literature report, with *a* = 4.581(4) Å and *c* = 8.998(2) Å. In this structure, the Cu(I) cation is accommodated in a tetrahedral coordination geometry rather than the more common linear O–Cu–O coordination geometry, but similar to that in the recently reported metastable $Cu_2Nb_8O_{21}$ compound.[16]

Compounds in these Cu(I)-containing systems are typically unstable towards either disproportionation or oxidation reactions at their surfaces when heated under vacuum or in air, respectively, such as when prepared as polycrystalline *p*-type films. This results in highly Cu-deficient compositions such as $Cu_{5-x}Ta_{11}O_{30}$ and $Cu_{1-x}Nb_3O_8$.[22,23] Prior electronic structure calculations on Cu_3VO_4 have found that Cu-vacancy formation occurs at relatively low energies, leading to the facile formation of a Cu-deficient composition.[26] To investigate the conditions for

preparing *p*-type Cu_3VO_4 polycrystalline films, the compound was heated under vacuum at 400 ^oC for 3 h, followed by heating in air at 300 ^oC or 350 ^oC for 15 min. After annealing at 400 ^oC in vacuum, scanning electron microscopy (SEM) images of the Cu_3VO_4 powder showed large micron-sized particles with smooth surfaces (see Figure S2). Upon heating this product to either 300 ^oC or 350 ^oC in air, thermogravimetric analyses (see Figure S3) show a weight gain of 2.86% (and climbing) and 5.76% (plateau reached) after 15 min, respectively. Concomitantly, the refined *a*-axis and *c*-axis unit-cell dimensions from the PXRD data, Figure 2, decrease at both temperatures by a similar 0.012 Å (0.26%) and 0.026 Å (0.29%), respectively. This is consistent with the partial extrusion of Cu(I) cations and the formation of CuO islands at the surfaces, as given in Reaction 1. This reaction apparently occurs finely over all of the particles' surfaces, and not preferentially over only some of the crystal facets, as shown in the SEM images in Figure 3(c-f). The weight gain measured by thermogravimetric analysis results in a calculated $x \sim 0.55$, or a Cu-deficiency corresponding to a composition of $Cu_{\sim 2.45}VO_4$. Consistent with this, preliminary Rietveld refinement results of the PXRD pattern confirms the presence of Cu-vacancies and a refined composition of $Cu_{2.52(2)}VO_4$ ($x \sim 0.48(2)$), with the full structural details and electronic structure calculations to be reported in a separate investigation.

$$Cu_3VO_4(s) + (x/2)\,O_2(g) \rightarrow Cu_{3-x}VO_4(s) + x\,CuO(surface) \qquad \text{(Reaction 1)}$$

$$2\,Cu_{3-x}VO_4(s) + (1.5-x)\,O_2(g) \rightarrow Cu_3V_2O_8(s) + (3-2x)\,CuO(s) \qquad \text{(Reaction 2)}$$

At a temperature of 300 ^oC only pure $Cu_{3-x}VO_4$ is observed by powder XRD (with shifted lattice parameters), while after 15 min at 350 ^oC the two Cu(II)-containing phases CuO and $Cu_3V_2O_8$ both appear in small amounts in Figure 2. These surface features are clearly visible in the SEM images in Figure 3 (c and d), and which grow substantially after 120 min in air at 350 ^oC in Figure 3 (e and f). The $Cu_3V_2O_8$ phase grows as long rod-like needles that emanate from

the surfaces with widths of ~15 to 25 nm and lengths of up to ~5 μm. Energy dispersive spectroscopy (EDS) data, Figure 4 (c and d), show that the long rod-like needles contain a significantly higher amount of vanadium content compared to the EDS data collected normal to the surfaces, i.e., corresponding to $Cu_3V_2O_8$ and CuO, respectively. However, a more accurate measurement of the surface compositions could not be obtained in the EDS analyses as it was not possible to locate clearly differentiated and ideal flat surfaces for each of the two surface nanoparticle phases. Thus, the slightly higher temperature results in the greater surface decomposition and oxidation of the $Cu_{3-x}VO_4$ phase into $Cu_3V_2O_8$ and CuO in an overall 1:3 molar ratio, respectively, as represented by Reaction 2. Importantly, these surface features are found to play a critical role in enhancing the photocurrents of the *p*-type Cu_3VO_4 films, as described below.

B. Optical and Photoelectrochemical Properties. Previous research in the Cu(I)-tantalate and Cu(I)-niobate systems has revealed several new *p*-type semiconductors with visible-light bandgap sizes spanning the range from ~1.5 eV to ~2.6 eV, including $CuNbO_3$, $CuNb_3O_8$ and $Cu_5Ta_{11}O_{30}$.[12-16] These bandgap sizes are found to be determined primarily by a metal-to-metal charge transfer between the filled Cu $3d^{10}$ orbitals and the empty Nb/Ta $4d^0/5d^0$ orbitals that make up the valence and conduction bands, respectively. However, recent results and calculations have suggested that even smaller bandgap sizes are possible in the Cu(I)-vanadate system, owing to the relatively lower-energy of the V $3d^0$ orbitals. A UV-Vis diffuse reflectance spectrum was taken on the pure Cu_3VO_4 powder, as shown in Figure 5. A bandgap size of ~1.17 eV for Cu_3VO_4 can be extracted from the linear rise in absorption. Tauc plots of the indirect and direct bandgap transitions yield values of ~1.14 eV and ~1.17 eV, respectively, as plotted in Figure S4 in the Supporting Information. This compares to a recently calculated

value for its bandgap size of ~1.0 eV.[26] This bandgap size is less than that required thermodynamically for total water splitting by a single semiconductor (i.e., 1.23 eV for $H_2(g)$ + ½ $O_2(g)$ → $H_2O(g)$). However, the band energies are potentially suitable for utilization within tandem photoelectrochemical cells that combine both *p*-type and *n*-type semiconductors, i.e., having a conduction band that is located suitably negative of the water reduction potential. After heating the Cu_3VO_4 phase to 300 ^oC and 350 ^oC, their UV-Vis diffuse reflectance spectra show the emergence of an additional absorption edge at ~800 nm, shown in Figure 6, which matches closely with that measured for both $Cu_3V_2O_8$ and CuO (i.e., compare to Figure S5 in Supporting Information).

Photoelectrochemical measurements were performed on polycrystalline Cu_3VO_4 films in order to investigate its photocurrent response under visible-light irradiation and the energies of its conduction and valence band edges. Linear-sweep voltammetry measurements of the Cu_3VO_4 films were carried out under chopped visible-light irradiation for an applied bias range of +0.2 V to –0.2 V vs. SCE, as shown in Figure 7. For the polycrystalline Cu_3VO_4 film not heated in air, a relatively large dark current and small cathodic photocurrent were observed that increased with the negative potential bias, up to ~0.015 mA/cm^2, indicating *p*-type behavior of the film in the depletion condition. After heating Cu_3VO_4 films to 300 ^oC and 350 ^oC, significantly larger cathodic photocurrents were observed that increased to ~0.06 mA/cm^2 and ~0.1 mA/cm^2, respectively, at a zero applied bias. At a larger negative applied bias of –0.2 V, higher cathodic photocurrents of up to ~0.25 mA/cm^2 and ~0.1 mA/cm^2 are observed. In addition, in each case the dark current is significantly reduced after heating the film in air. At a larger irradiant power density of ~500 mW/cm2 (λ > 420 nm) even higher photocurrents (×2 – 3) can be obtained, as shown in Figure S10 in the Supporting Information. PXRD data of the Cu_3VO_4 films show no

apparent changes after each of the photocurrent measurements, with refinements on the diffraction peaks yielding no detectable changes in the lattice constants. The formation of the CuO and $Cu_3V_2O_8$ particles on the surfaces are thus shown to have a significant impact of increasing the photocurrent response of the Cu_3VO_4 films.

The effects of the surface nanoparticles on the cathodic photocurrents of $Cu_{3-x}VO_4$ films were investigated independently of the Cu-site vacancies that form when heated in air. Following previously reported procedures,[23] nanoparticles of CuO were deposited onto the surfaces of Cu_3VO_4 films using 0.1M and 0.25M aqueous solutions of $Cu(NO_3)_2$ and heating at 250 ^oC for 20 min, yielding ~4% (0.4 mg) and ~10% (1.0 mg) CuO by weight. Scanning electron microscopy images of the prepared films, Figure 8, show the expected formation of CuO surface nanoparticles as confirmed by PXRD data (Figure S7 in the Supporting Information). The 0.1 M $Cu(NO_3)_2$ solution yielded surface nanoparticles with sizes of ~20 to 40 nm with a surface coverage of ~50 to 75%, while a more complete coverage of the surfaces is obtained using the 0.25 M $Cu(NO_3)_2$ solution and with much larger particle sizes of > ~250 nm. Linear sweep voltammetry of these films show cathodic photocurrents of ~0.2 mA/cm^2, shown in Figure 9 (left), and that are similar or larger than the photocurrent response found for the $Cu_{3-x}VO_4$ films after heating in air. Plotted in Figure 9 (right), chronoamperometric measurements also show a photocurrent that becomes relatively stabilized after a period of ~4000 s. Thus, these results confirm the key role of surface CuO nanoparticles in enhancing the photocurrent density of the Cu_3VO_4 films.

An analogous route to preparing surface $Cu_3V_2O_8$ nanoparticles on these films has not been found. However, as the $Cu_{3-x}VO_4$ films with a mixture of CuO and $Cu_3V_2O_8$ surface nanoparticles exhibit a relatively smaller photocurrent than the Cu_3VO_4 films with CuO alone,

this suggests that the $Cu_3V_2O_8$ nanoparticles have a similar or negligible contribution. Further, when the Cu_3VO_4 films are heated to 350 ^oC for 120 min, yielding the largest amounts of surface $Cu_3V_2O_8$, very small to negligible photocurrents are measured (given in Figure S9 in the Supporting Information).

Mott-Schottky measurements were performed in order to determine the conduction and valence band energies, and involves a measurement of the film capacitance (C) as a function of the applied photoelectrode potential (V), as shown in Figure 10. The negative slope of $1/C^2$ versus V shows the expected behavior for a *p*-type semiconductor. The linear region can be extrapolated to obtain the *x*-axis intercept (V_0 = -0.19 V versus SCE, or +0.40 V versus RHE at pH = 5.8). For *p*-type semiconductors, the valence band energy (E_V) can be calculated from the flat-band potential (V_{fb}) with the equation, $E_v = V_{fb} + kT \ln(N_A/N_V) - kT/e^2$, where N_A is the acceptor concentration and N_V is the effective density of states (typically ~ 10^{19}) at the valence band edge, k is the Boltzmann constant, T is temperature, and *e* is the electron charge.[35] The value of the acceptor density, N_A, from the Mott-Schottky plot was found to be ~1.3×10^{17} cm^{-3}. This yields a valence band position of +0.54 V versus RHE (pH = 5.8). Adding the bandgap size to the valence band position gives the conduction band position at –0.63 V under these conditions. The conduction band energy of Cu_3VO_4 is thus ~ 300 mV more negative than the (H^+/H_2) redox couple. This is also at a slightly more negative potential than in CuO, which has previously been determined to fall in the range of –0.5 V to –0.6 V, depending on the preparation conditions and after calibrating for pH (~59 mV per unit) and different reference electrodes.[22,36] This band-energy offset facilitates the transfer of excited electrons from Cu_3VO_4 to CuO, followed by the reduction of protons at the surfaces of CuO. Conversely, the valence band energy of CuO has previously been found to be at a more positive potential of +0.6 V to +0.7 V,

and therefore inhibiting hole migration from the valence band in Cu_3VO_4 to CuO. Thus, a type-II band offset is formed between *p*-type CuO and *p*-type Cu_3VO_4, and which would lead to a rectification of charge-transport at the surfaces and an increased efficiency of charge separation. Analogous band-energy measurements have not been reported for $Cu_3V_2O_8$.

C. Electronic Structure Calculations. Electronic structure calculations were performed using the previously reported Cu_3VO_4 crystal structure. Consistent with prior results,[26] the calculated densities-of-states (Figure S8 in the Supporting Information) show that the conduction and valence band states at the band edges consist primarily of the V $3d^0$-orbital and Cu $3d^{10}$-orbital contributions, respectively, with a smaller amount of contributions from the O 2*p* orbitals. Thus, visible-light excitation of electrons from the valence to the conduction band states corresponds to a Cu-to-V charge transition within the structure. Illustrated in Figure 11 is an electron density plot for Cu_3VO_4 at the lowest-energies of the conduction band (yellow shading in a and c) and highest-energies of the valence band (blue shading in b). The lowest-energies of the conduction band states are delocalized over the vanadium and oxygen atoms in the $[CuVO_4]_\infty$ layers within the *ab*-plane, as shown in Figure 11c. Conversely, the highest-energy electron density in the valence band is delocalized over the copper atoms within both the $[CuVO_4]_\infty$ and $[Cu_2O_4]_\infty$ layers, and is thus delocalized throughout the full three-dimensional structure.

The calculated band structure diagram (i.e. *k* versus energy) is plotted in Figure 12, with the minimum-energy indirect bandgap transition labeled. The band gap is predicted to be indirect and to occur between *k*-points N and G (i.e., G = gamma point), with a slightly higher-energy direct bandgap transition at the G *k*-point. The bandgap size of Cu_3VO_4 is under-estimated by these methods by around ~1 eV, as has been documented previously for Cu(I)-

containing oxides.[26,37] Interestingly, the conduction bands show a significant dispersion around the G *k*-point of ~2 eV, resulting in a smaller densities-of-states at the bottom of the conduction band, as shown by comparing Figures 12 and S8. The joint densities-of-states, and thus the optical absorption, is much smaller at the lowest-energies of the conduction band. The large band dispersion of the conduction band also suggests a high mobility of the photoexcited electrons, as the effective mass of the electron is proportional to $(1/d^2E/dk^2)$. This large dispersion is a result of the non-bonding V *d*-orbitals (i.e, d_{x2-y2}, d_{z2} set) at the G *k*-point, but which rapidly mix in an antibonding fashion with the O 2*p* orbitals when moving away from the G *k*-point. This can be seen in the partial densities-of-states in Figure S8, wherein the contributions from the O 2*p*-orbitals increase towards the higher-energies of the conduction band. By contrast, the band dispersion within the valence band is relatively much smaller, at ~0.5 eV, when moving away from the N *k*-point. This results in a higher mobility for the excited electrons than for the holes, leading potentially to higher charge recombination rates and reduced photocurrents. Thus, the rectifying CuO/Cu_3VO_4 interfaces at the surfaces play an important role in both reducing the dark current and in achieving a significant enhancement in the *p*-type photocurrent.

V. CONCLUSIONS

A *p*-type semiconductor in the Cu(I)-vanadate system, Cu_3VO_4, has been investigated for its small optical bandgap size (E_g ~ 1.2 eV) and photoelectrochemical properties in the form of *p*-type polycrystalline films. Upon heating the films in air, the compound exhibits a Cu-deficient composition of $Cu_{3-x}VO_4$(s) (x ~ 0.48(2)), as found by powder X-ray diffraction and thermogravimetric analyses. At 350 ^oC the compound partially decomposes at its surfaces into

the Cu(II)-containing oxides CuO and $Cu_3V_2O_8$ (3:1 molar ratio). When polycrystalline films of *p*-type Cu_3VO_4 were prepared under these same conditions, high cathodic photocurrents are found under visible-light irradiation (AM 1.5 G filter) when compared to films not heated in air. The conduction band potential of the Cu_3VO_4 film was found to be at ~ –0.63V versus RHE at pH = 5.8, which is slightly more negative than the conduction band of CuO. The bandgap transition is predicted to be indirect, originating from an excitation between the filled Cu $3d^{10}$ and empty V $3d^0$ orbitals, with a large dispersion of the conduction band states near the G *k*-point in the band structure. The deposition of surface CuO nanoparticles onto Cu_3VO_4 films (not heated in air) showed similar to higher photocurrents as compared to the films heated in air. Thus, the nanoparticle CuO surface islands were found to play a key role in forming a charge rectification layer at the surfaces of the Cu_3VO_4 photoelectrode films, yielding the strong enhancements in its *p*-type photocurrent after heating in air. Further structural and photoelectrochemical investigations are currently underway in order to provide more detailed insights into the properties of these small bandgap Cu(I)-containing *p*-type photoelectrodes, and which are relevant for uses in tandem *n*-type/*p*-type solar cell configurations.

VI. SUPPORTING INFORMATION

For Cu_3VO_4, a whole-pattern fitting of its powder X-ray diffraction data, scanning electron microscopy images of a freshly-synthesized sample, thermogravimetric plots at 300 ^oC and 350 ^oC in air, Tauc plots of the direct and indirect bandgap transitions, photocurrent measurements of a polycrystalline film annealed in vacuum (no heating in air), powder X-ray diffraction patterns of the films before and after photocurrent measurements and before and after

the deposition of CuO surface nanoparticles, calculated densities-of-states plot, and a written description of the Mott-Schottky calculations. This material is available free of charge *via* the internet at http://pubs.rsc.org.

VII. ACKNOWLEDGMENTS

The authors acknowledge support of this research from the National Science Foundation (DMR-0644833) and the Department of Chemistry at North Carolina State University. Dr. Mooney and Garcia in the Analytical Instrumentation Facility at North Carolina State University are also acknowledged for their assistance in the collection of SEM data.

VIII. REFERENCES

1. F.E. Osterloh, *Chem. Mater.* 2008, **20**, 35–54.

2. R. Abe, *J. Photochem. Photobiol. C* 2010, **11**, 179-209.

3. A. Fujishima, K. Honda, *Nature* 1972, **238**, 37.

4. U. A. Joshi, A. Palasyuk, D. Arney, P. A. Maggard, *J. Phys. Chem. Lett.* 2010, **1**, 2719-2726.

5. A. Kudo, Y. Miseki, *Chem. Soc. Rev.* 2009, **38**, 253-278.

6. J. H. Kennedy, K. W. Frese, *J. Electrochem. Soc.* 1978, **125**, 709-714.

7. G. Hodes, D. Cahen, J. Manassen, *Nature* 1976, **260**, 312-313.

8. I. Shintaro, K. Yamada, T. Matsunaga, H. Hagiwara, Y. Matsumoto, T. Ishihara, T. *J. Am. Chem. Soc.* 2010, **132**, 17343-17345.

9. M. Hara, T. Konda, M. Komoda, S. Ikeda, K. Shinohara, A. Tanaka, J. N. Konda, K. Domen, *Chem. Commun.* 1998, 357-358.

10. W. B. Ingler, J. P. Baltrus, S. U. M. Khan, *J. Am. Chem. Soc.* 2004, **126**, 10238-10239.

11. C. Leygraf, M. Hendewerk, G. A. Somorjai, *J. Phys. Chem.* 1982, **86**, 4484-4485.

12. P. P. Sahoo, P. A. Maggard, P.A. *Inorg. Chem.* 2013**, 52**, 4443-4450.

13. U. A. Joshi, A. Palasyuk, P. A. Maggard, *J. Phys. Chem. C* 2011, **115**, 13534-13539.

14. U. A. Joshi, P. A. Maggard, *J. Phys. Chem. Lett.* 2012**, 3**, 1577-1581.

15. L. Fuoco, U. A. Joshi, P. A. Maggard, *J. Phys. Chem. C* 2012, **116**, 10490-10497.

16. J. Choi, N. King, P. A. Maggard, *ACS Nano* 2012, **7**, 1699-1708.

17. O. Palasyuk, A. Palasyuk, P. A. Maggard, *J. Solid St. Chem.* 2010, **183**, 814-822.

18. Z. Zhang, P. Wang, *J. Mater. Chem.* 2012, **22**, 2456-2464.

19. Q. Huang, F. Kang, H. Liu, Q. Li, X. Xiao, *J. Mater. Chem. A* 2013, **1**, 2418-2425.

20. H. Chen, W. Leng, Y. Xu, *J. Phys. Chem. C* 2014, **118**, 9982-9989.

21. R. Patil, S. Kelkar, R. Naphade, S. Ogale, *J. Mater. Chem. A* 2014, **2**, 3661-3668.

22. N. King, P. P. Sahoo, L. Fuoco, S. Stuart, D. Dougherty, Y. Liu, P. A. Maggard, *Chem. Mater.* 2014, **26**, 2095-2104.

23. I. Sullivan, P. P. Sahoo, L. Fuoco, A. Hewitt, S. Stuart, D. Dougherty, P. A. Maggard, *Chem. Mater.* 2014, **26**, 6711-6721.

24. a) A. J. Nozik, *Appl. Phys. Lett.* 1976, **29**, 150-153; b) S. Hu, C. Xiang, S. Haussener, A. D. Berger, N. S. Lewis, *Energy Environ. Sci.* 2013, **6**, 2984-2993.

25. N. Barrier, M. Hervieu, N. Nguyen, B. Raveau, *Solid St. Sci.* 2008, **10**, 137-140.

26. G. Trimarchi, H. Peng, J. Im, A. Freeman, V. Cloet, A. Raw, K. Poeppelmeier, K. Biswas, S. Lany, A. Zunger, *Phys. Rev. B* 2011, **84**, 165116-1-165116-14.

27. M. Dusek, V. Petricek, M. Wunschel, R. E. Dinnebier, S. van Smaalen, S., *J. Appl. Crystallogr.* 2001, **34**, 398-404.

28. P. Kubelka, F. Munk, *Z. Tech. Phys*. 1931, **12***,* 593.

29. J. Tauc (F. Abeles ed.), *Optical Properties of Solids*, North-Holland, 1972.

30. a) G. Kresse, G. Hafner, *Phys. Rev. B* 1993, **47(1)**, 558-561; b) *Ibid*, 1994, **49(20)**, 14251-14270; c) G. Kresse, J. Furthmüller, *Comput. Mat. Sci*. 1996, **6(1)**, 15-50; d) G. Kresse, J. Furthmüller, *Phys. Rev. B* 1996, **54(16)**, 11169-11186.

31. J. P. Perdew, K. Burke, M. Ernzerhof, *Phys. Rev. Lett.* 1996, **77(18)**, 3865-3868.

32. a) P. E. Blöchl, *Phys. Rev. B* 1994, **50(24)**, 17953-17979; b) G. Kresse, D. Joubert, *Phys. Rev. B* 1999, **59(3)**, 1758-1775.

33. H. J. Monkhorst, J. D. Pack, *Phys. Rev. B* 1976, **13**, 5188-5192.

34. W. Setyawan, S. Curtarolo, *Comput. Mater. Sci.* 2010, **49(2)**, 299-312.

35. W. P. Gomes, F. Cardon, *Prog. Surf. Sci.* 1982, **12**, 155-216.

36. F. P. Koffyberg, F. A. Benko, *J. Appl. Phys.* 1982, **53(2)**, 1173-1177.

37. M. Harb, D. Masih, K. Takanabe, *Phys. Chem. Chem. Phys.* 2014, **16**, 18198-18204.

Table 1. Refined unit-cell lattice parameters from powder X-ray diffraction data on Cu_3VO_4.[a]

Sample	*a* (Å)	*c* (Å)	Volume (Å^3)
Literature values	4.57531(9)	8.9918(3)	188.229(7)
As synthesized	4.581(4)	8.998(2)	188.82(4)
Heated 400 ^{o}C in vacuum	4.569(1)	8.972(6)	187.3(1)
Heated 300 ^{o}C in air	4.569(1)	8.972(5)	187.3(1)
Heated 350 ^{o}C in air	4.569(1)	8.973(6)	187.8(3)

[a] Tetragonal crystal system, Space Group I-42*m* (No. 121); Samples were heated under similar conditions as the film preparation conditions.

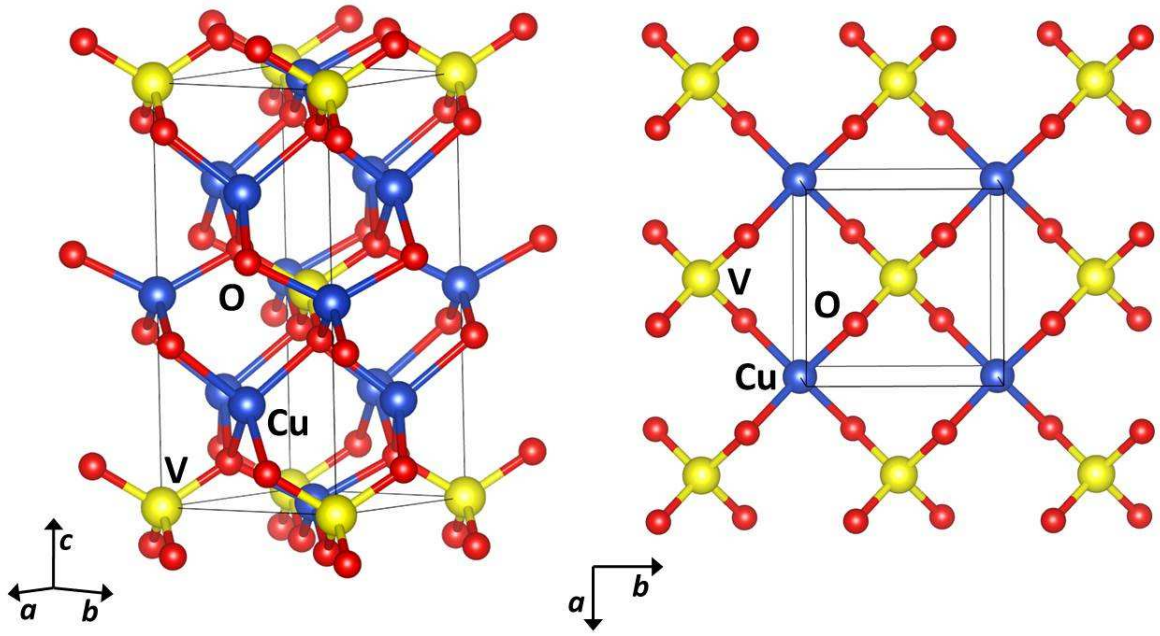

Figure 1. Overall unit-cell view of Cu_3VO_4 (left), and of a single $[CuO_{4/2}VO_{4/2}]$ layer (right), with representative atom types and the coordinate axes labeled in each.

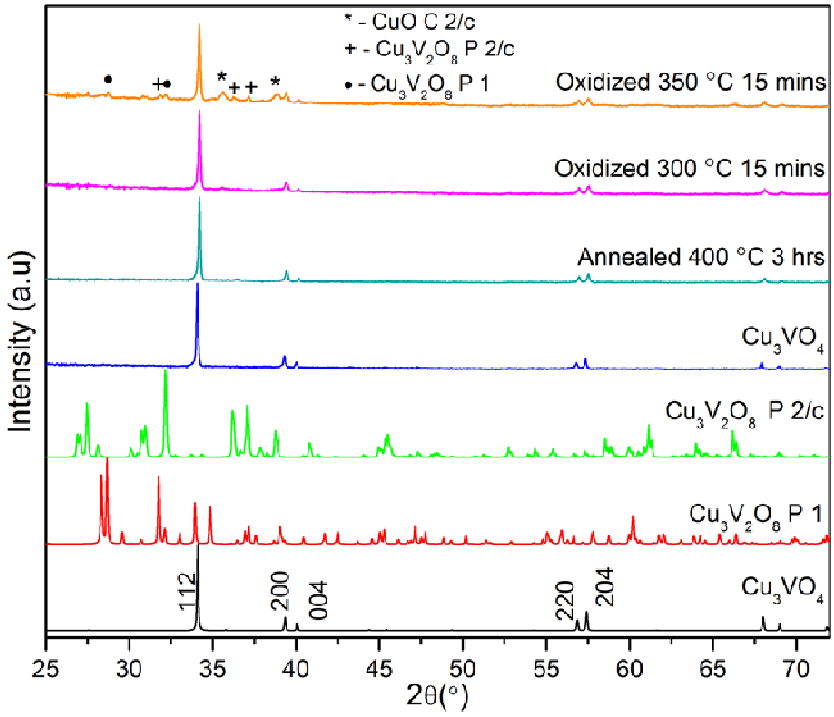

Figure 2. Powder X-ray diffraction patterns of the freshly-prepared Cu_3VO_4, and after annealing at 400 °C, and followed by heating at 300 °C and 350 °C. Calculated patterns for Cu_3VO_4 and $Cu_3V_2O_8$ (two types) are shown at the bottom, for comparison.

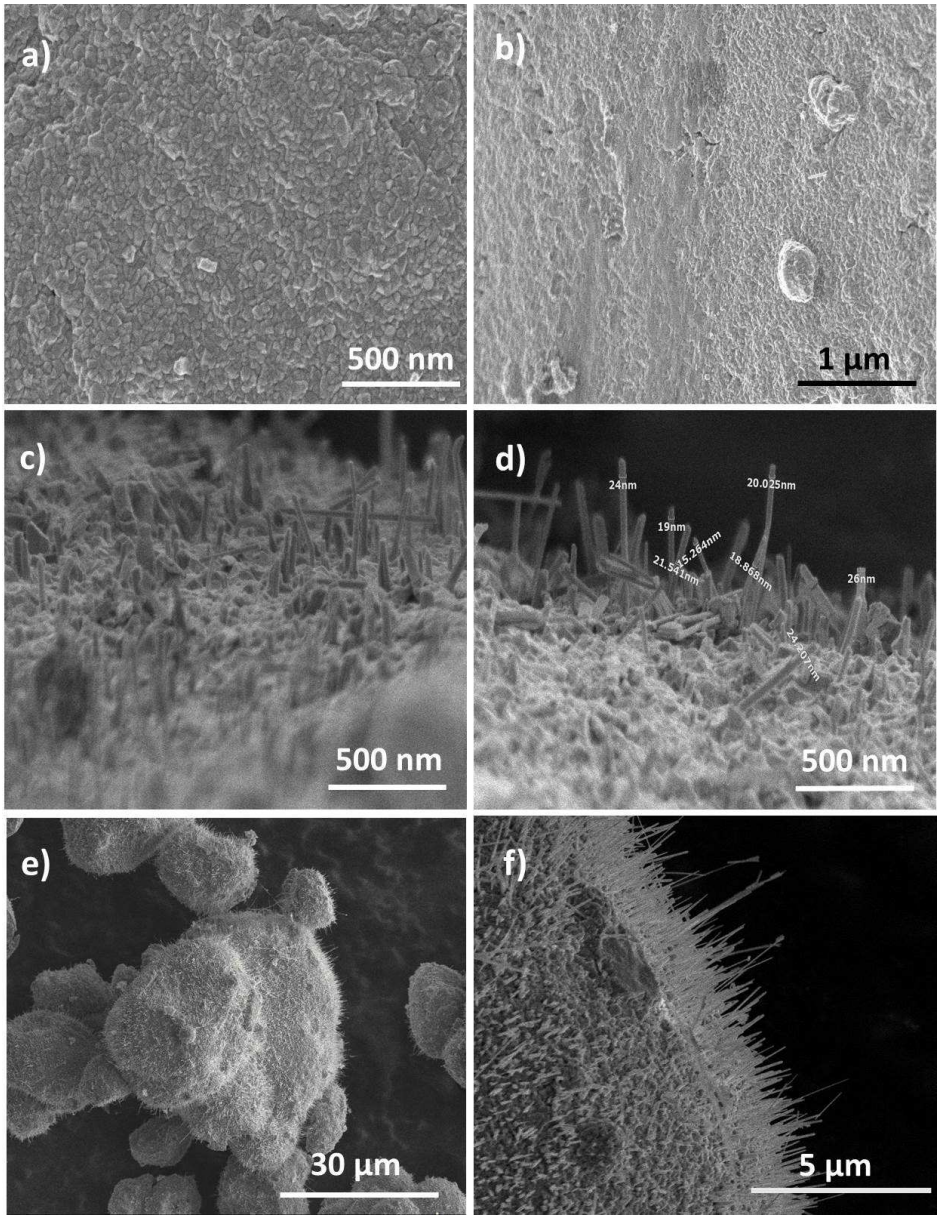

Figure 3. Scanning electron microscopy images of the surfaces of Cu_3VO_4 particles after annealing at 400 ^oC, followed by heating in air at 300 ^oC for 15 min (a, b), or at 350 ^oC for 15 min (c, d), or at 350 ^oC for 120 min (e, f).

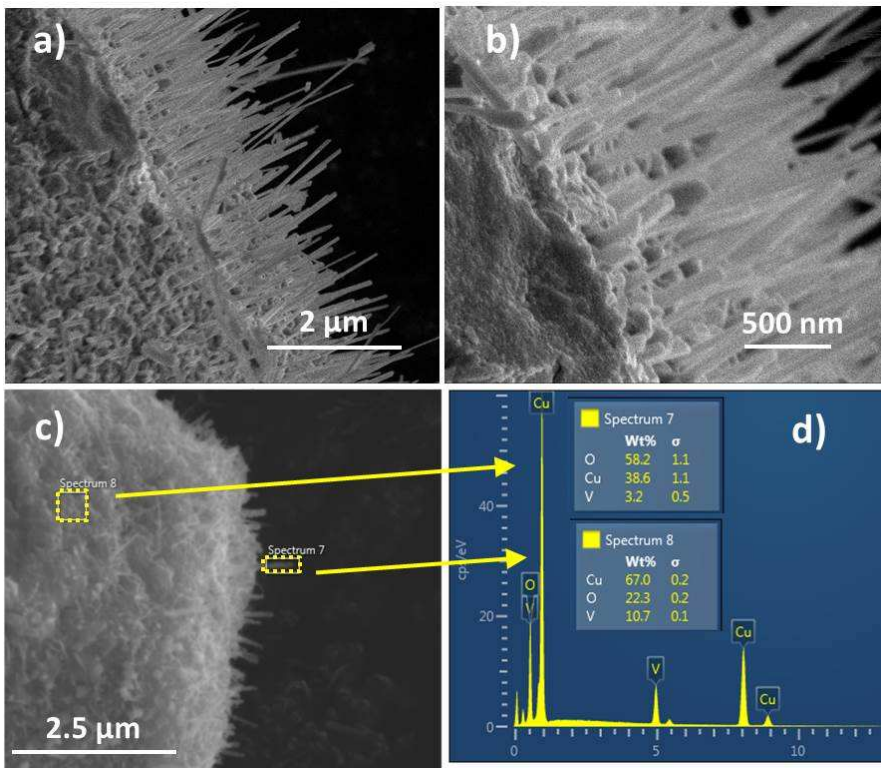

Figure 4. Higher-magnification scanning-electron microscopy images of the surfaces of a Cu_3VO_4 particle after annealing at 400 ^oC followed by heating in air at 350 ^oC for 120 min (a, b), and energy dispersive spectroscopy of a particle after heating in air at 350 ^oC for 15 min (c, d).

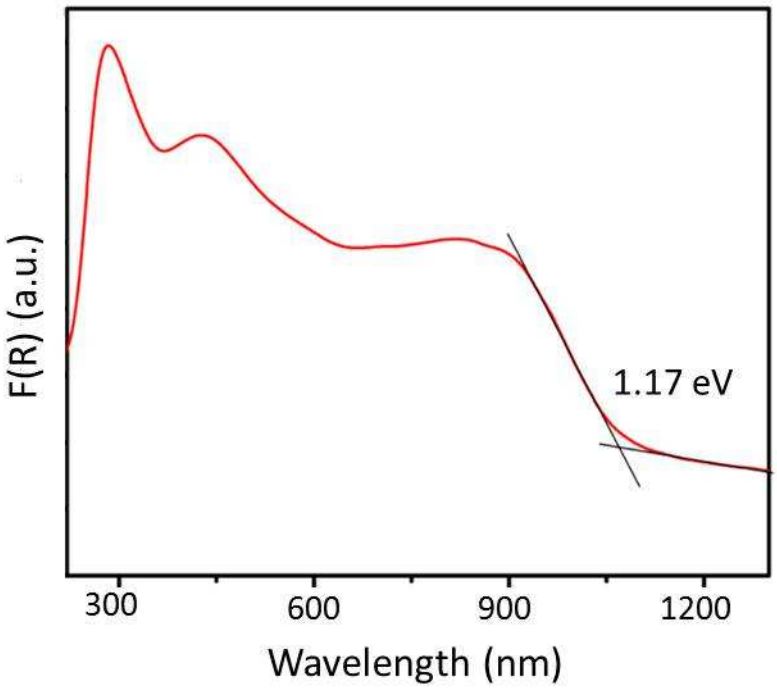

Figure 5. UV-Vis diffuse reflectance spectrum of freshly-prepared Cu_3VO_4, plotted as the Kubelka-Munk function versus wavelength.

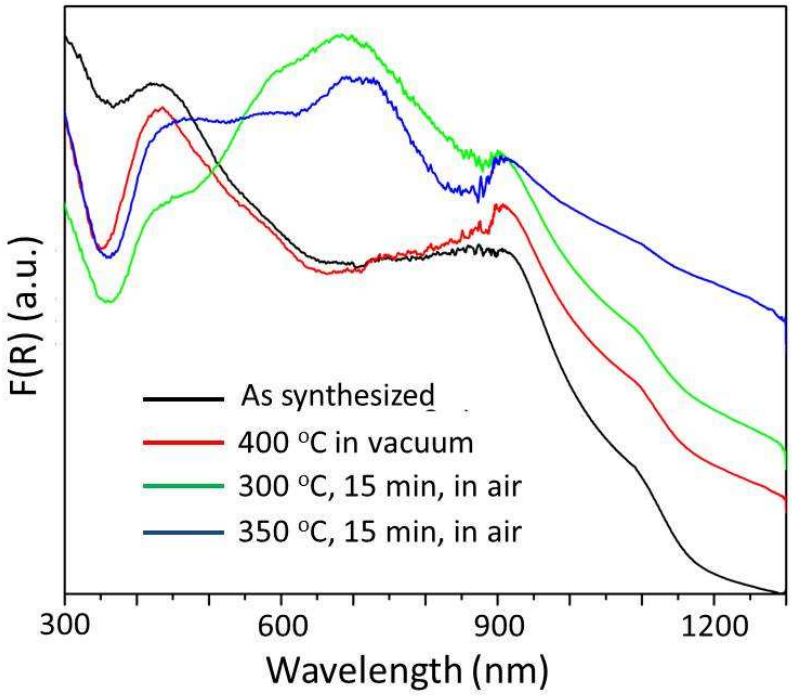

Figure 6. Comparison of the UV-Vis diffuse reflectance spectra, plotted as the Kubelka-Munk function versus wavelength, for freshly-prepared Cu_3VO_4 (black), after annealing at 400 °C for 3 h (red), and subsequently heated in air at 300 °C (green) or 350 °C (blue) for 15 min.

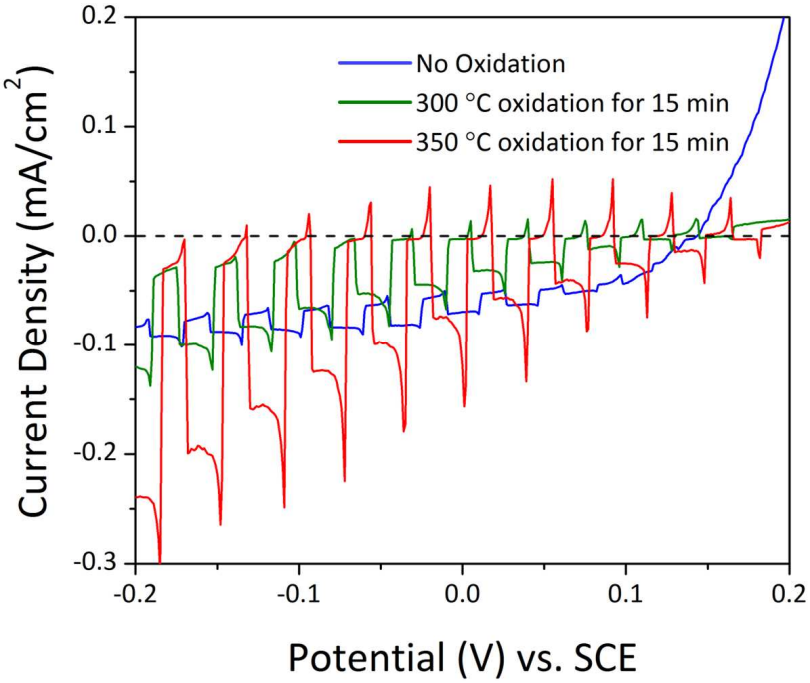

Figure 7. Current-potential curve for polycrystalline $Cu_{3-x}VO_4$ films in an aqueous 0.5 M Na_2SO_4 solution (pH = 5.8) under chopped visible-light irradiation. The films were annealed at 400 ºC for 3h, followed by either no further heating (blue), or heating in air for 15 min at 300 ºC (green) or 350 ºC (red).

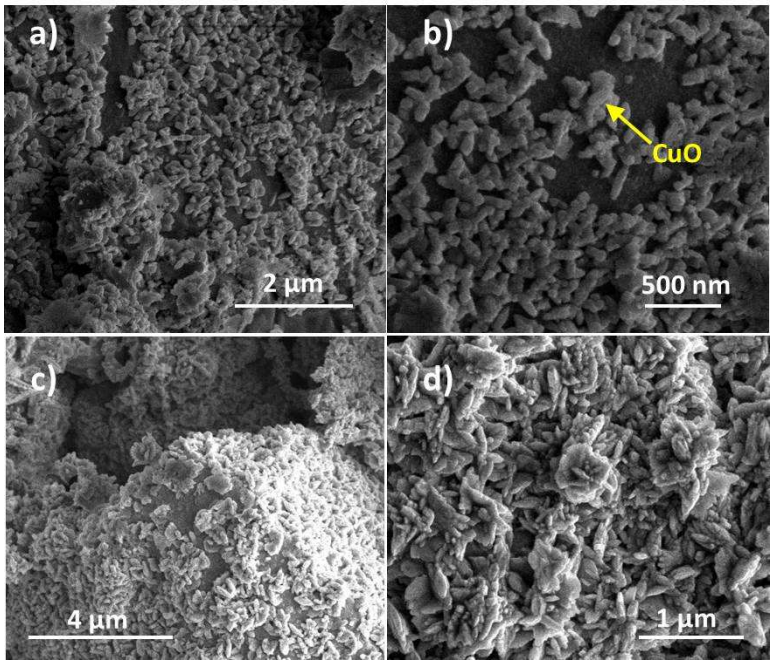

Figure 8. Scanning electron microscopy images of the surfaces of Cu_3VO_4 particles after the deposition of CuO nanoparticles from aqueous 0.1M (a, b) and 0.25 M (c, d) solutions of $Cu(NO_3)_2$.

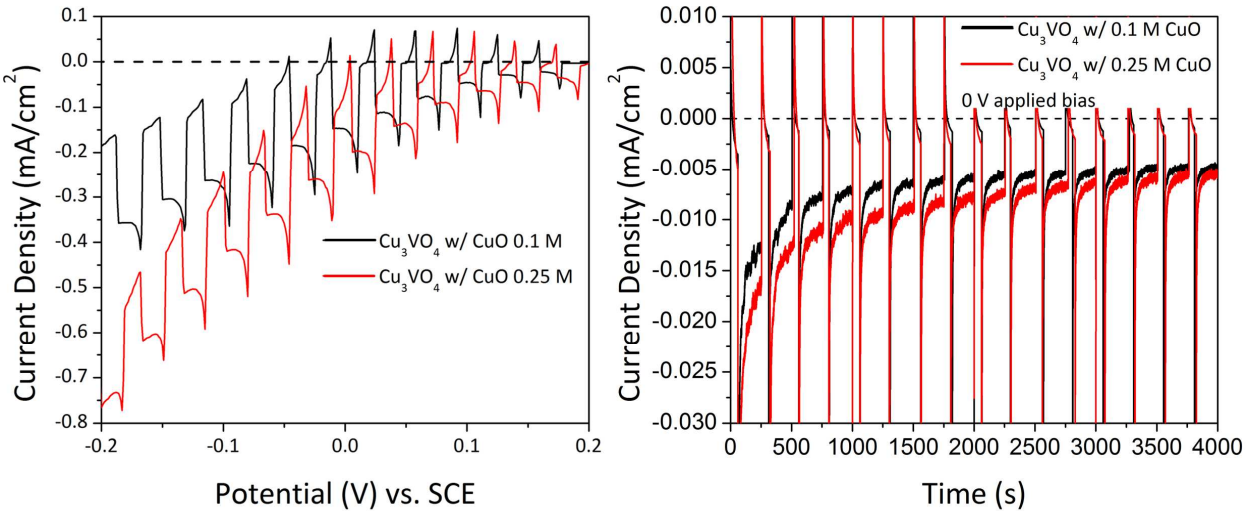

Figure 9. Current-potential (left) and current-time measurements (right) for polycrystalline Cu_3VO_4 films with CuO nanoparticles deposited onto their surfaces using a $Cu(NO_3)_2$ aqueous solution (0.1M or 0.25M). Measurements were performed in an aqueous 0.5 M Na_2SO_4 solution (pH = 5.8) under chopped visible-light irradiation.

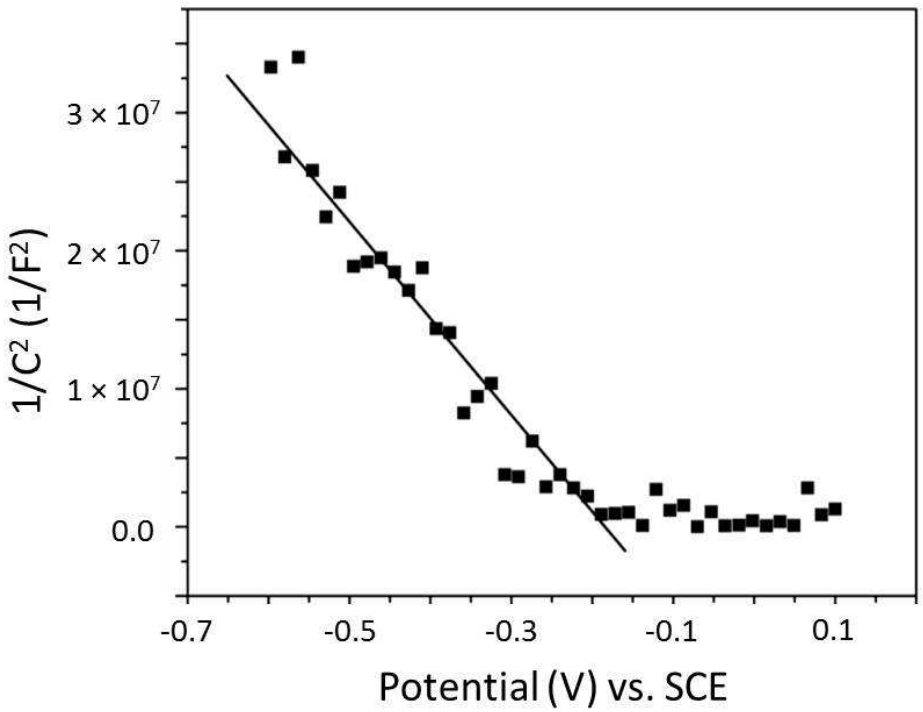

Figure 10. Mott-Schottky plot (inverse capacitance squared (C^{-2}) versus potential (V)) for a polycrystalline Cu_3VO_4 film annealed at 400 ºC.

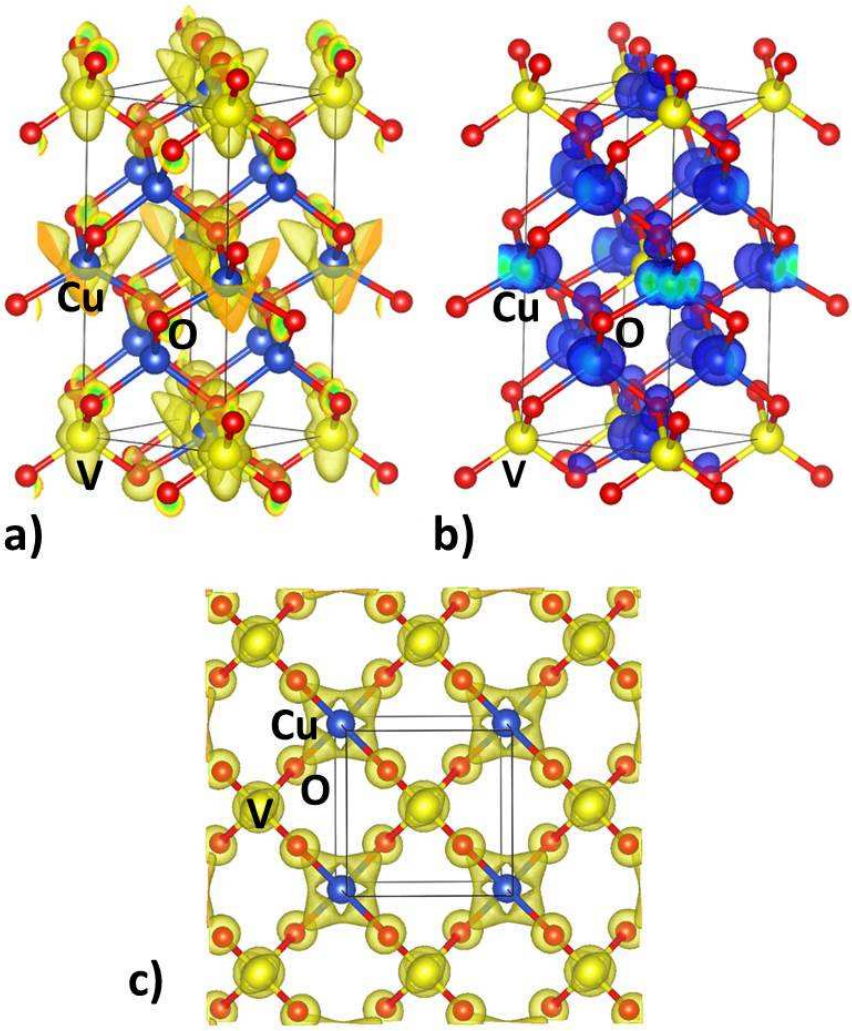

Figure 11. Calculated electron density for Cu_3VO_4 at the lowest-energies of the conduction band (yellow shading in a and c) and highest-energies of the valence band (blue shading in b), with the unit cells and atom types labeled. Orientation of the unit cells are the same as illustrated in Figure 1.

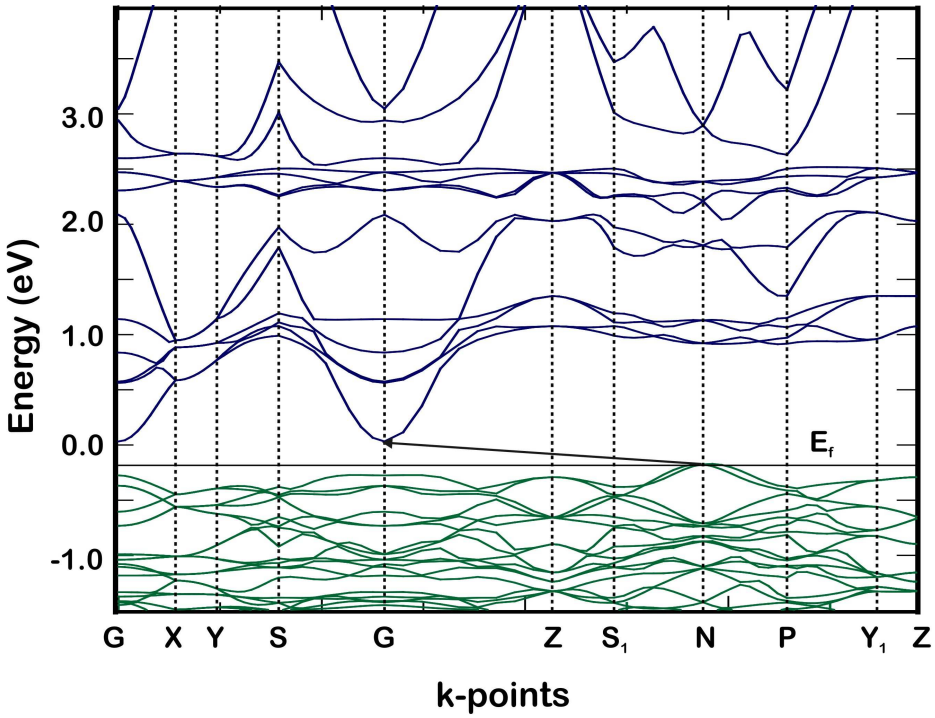

Figure 12. The calculated band structure (i.e., k-point versus energy) for the standard *k*-path for a body-centered tetragonal crystal system (criterion *c*-axis > *a*-axis) given in Ref. 34: Γ-X-Y-Σ-Γ-Z-Σ_1-N-P-Y_1-Z. The Fermi level (E_f) and the lowest-energy indirect bandgap transition are both labeled.

Table of Contents Figure and Short Caption

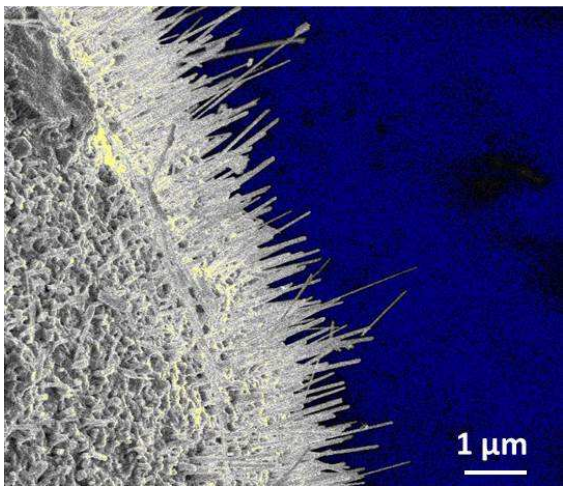

TOC caption: Formation of surface nanoparticles on *p*-type Cu_3VO_4 (shown) and their critical role in enhancing its photocurrents for solar energy conversion.